Analysis
of
JEM-X background effects

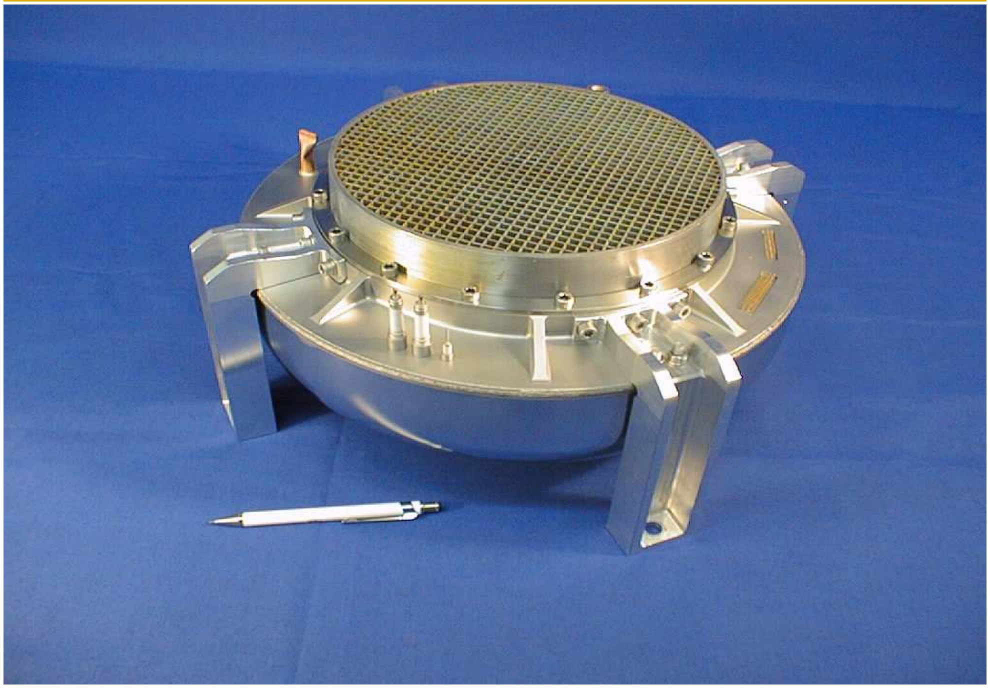

Jakob Hansen Jon Gaarsmand

Copenhagen
May 3, 1999

The front page shows the coded mask used for JEM-X and the detector unit with collimator (Courtesy of DSRI).

Bachelorproject:

Analysis of JEM-X background effects

The contributions to this report are divided as follows:

Introduction	Jakob Hansen and Jon Gaarsmand have contributed equally to the introduction
Chapter 1	Jon Gaarsmand is responsible for this chapter
Chapter 2	Jakob Hansen is responsible for sections 2.2 and 2.3.
	Jon Gaarsmand is reponsible for section 2.4
Chapter 3	Jakob Hansen is responsible for this chapter
Chapter 4	Jakob Hansen is responsible for this chapter
Chapter 5	Jakob Hansen is responsible for sections 5.1,5.2, 5.3, 5.4 and 5.5.
	Jon Gaarsmand is responsible for section 5.6
	Jakob Hansen and Jon Gaarsmand have contributed equally to section 5.7
Chapter 6	Jakob Hansen and Jon Gaarsmand have contributed equally to this chapter

Jakob Hansen and Jon Gaarsmand

070675-2625 071076-1043

Internal supervisor:

Leif Hansen
Astronomical Observatory
Juliane Maries Vej 30
DK-2100 Copenhagen Ø
Denmark

External supervisor:

Niels Jørgen Westergaard
Danish Space Research Institute
Juliane Maries Vej 30
DK-2100 Copenhagen Ø
Denmark

Contents

Introduction (JG + JH)

In 2001 the INTEGRAL satellite will be launched by ESA. Onboard INTEGRAL is a X-ray monitor, JEM-X, that will operate in the energy interval 3 keV - 35 keV [15].

X-ray optics is, at the moment, useless at these energies, for which reason JEM-X is a coded mask telescope. A coded mask telescope is basically a plate with a large number of holes, that each works as a pinhole camera, projecting an image of the sky onto a detector. Thus, the detector image consists of a large number of overlapping images that need to be decoded before the skyimage can be viewed. Chapter 1 gives an introduction to the concept of coded mask cameras. The details of JEM-X is given in chapter 2.

In addition to point sources there are two other contributions that has an effect on the detector image, namely the diffuse X-ray background and the particle induced background. This background is expected to be non-uniformly distributed in the detector and to give rise to noise and false sources ("ghosts") in the decoded image [14],[12].

Knowledge of the effects this background has on the results is desireable in advance to the launch of the satellite. A software package, simulating the JEM-X detector [14], have been developed at the Danish Space Research Institute and can be used to analyse the effects of different assumptions. The simulation software is further described in chapter 3.

This report is concerned with the distribution of the background in the detector and the effects that a non-uniform background will have on the results, especially the amount and distribution of ghosts that it will inflict. Furthermore we wish to examine one method to reduce the effects of a non-uniform background, namely that of a low-pass filter. Chapter 4 analyses the distribution of the diffuse X-ray background. Chapter 5 is concerned with the expected distribution of the particle induced background and analyses the effects that various non-uniform particle induced backgrounds have on the decoded images.

Jakob Hansen (JH) and
Jon Gaarsmand (JG),
Copenhagen, May 1999

Chapter 1

Coded Aperture Cameras (JG)

For high energy astronomy observations with regular optical cameras is not possibly. Ground based astronomical apertures are "blinded" to the energy region of X-rays and γ-rays, because of the optical thickness of the atmosphere, which allmost absorbs all such radiation. Therefore space-borne observations are nescesarily.

Even for space observatories, there is a problem with low beam, and in order to focus the camera, only small detection windows (single pinhole) are possibly. The low beam throughput results in a very poor signal-to-noise ratio (SNR), and very long observations will be needed to make up for this.

Instead of making long observations one could try to increase the efficiency by enhancing the intensity of the flux through the detection window. One comprehensive way is to increase the number of pinholes and create several overlapping images of the observed object. However this type of imaging is not trivial, thus several overlapping images creates an image not very similar to the pictured. One need to reconstruct it comprehensively, which sets demands for the pattern of the pinholes and the reconstruction process. This is the nature of Coded apertures.

The image of overlapping shadows of the mask will be referred to as the shadowgram. Thus what is seen is the shadow of the mask illuminated by the sky onto the detector.

To achieve an image of the originally pictured image it will be necessary to reconstruct the image, by means of deconvolution or a correlation method, from the shadowgram.

Coded mask apertures are constructed with a mask, a plate with transparent, to the desired energy region, and opaque areas in a pattern, some distance above the camera. The reconstruction process or reconstruction algorithm is dependent on the design of the mask, the number of pinholes, the pattern of the pinholes, the size and shape of the mask and pinholes. This chapter will introduce various types of masks and image reconstruction methods, leading towards usefull constellations compatible with the prepared parts for JEM-X.

1.1 Mask Types and Design (JG)

More designs of mask patterns have been proposed. In the sixties Fresnel zonepattern and random pinhole pattern were proposed, however none of them was ideal through the non-flat sidelobes of their autocorrelation functions (will be introduced in 1.1.1). Later works based on random pinhole pattern have resulted in Uniformly Redundant Arrays (URA). Latest works have evolved to mask patterns with open fractions of less than 50% and two-scaled mask patterns.

Mask patterns with open fractions of less than 50% are thought to be superior in limiting the telemetry rate and, for point sources, optimizing the signal-to-noise ratio (SNR), real detection events from the sky modulated by the mask against noise arisen from background events (see section 1.4) or statistical and coding noise. SNR is normally needed high to segregate real sources from fluctuations as a result of non-uniform background or other noise.

Two-scaled mask patterns may consist of a low resolution pattern transparent for high energies, and a high resolution pattern only transparent for low energies in one mask. This construction has the adventage to be able to detect transient events in one scale and locate them in the other scale[11].

However neither one of the two has ideal autocorrelation functions yet[16].

1.1.1 Uniformly Redundant Arrays (URA)

Coded mask cameras with URA are basically pattern of cyclic difference set (characterized by integer parameters n, k and z), which means that any distance, less than some maximum, between pairs of transparent mask elements will only occur a constant number of times[3].

In the definition of URA is that the autocorrelation, the direct correlation applied to the mask, of a single peak on a flat background, will yield a δ-function.

Obtaining a δ-function means that no artifacts, like coding noise or source aliasing have arisen as a result of imperfect coding. This situation is optimum for a coded mask camera.

And the SNR is optimally as well. The latter is best obtained in a Hademard difference set, with integer t, where $n = 4t - 1$, $k = 2t - 1$ and $z = t - 1$.

This part of URAs has more undergroups, whereas the most important to this project is the Quadratic Residue Set, given by squares, modulo n of the first $(n+1)/2$, where n is a prime. Others are twin prime sets and pseudo-noise sets and a group called Singer sets[16].

URA coded masks are superior for use in high energy astronomy, both to single pinhole cameras, rastering collimators and other types coded masks, because of the δ-function obtained by the autocorrelation, and the compability to reconstruction methods.

1.2 Optical Design (JG)

Optical design of the coded mask camera also has an influence on the reconstruction and the quality of same. The Field Of View (FOV) and the angular resolution are decided by the design, through the distance and the difference in size between the mask and the detector[16].

The FOV is coded by the mask, however only a part is Fully Coded Field of View (FCFOV), in which all incoming photons are coded by the mask. The rest is in Partially Coded Field of View (PCFOV), where only some incoming photons, coded by the mask, will result in counts in the detector.

Often a collimator, instead of shielding, is used to restrict the FOV, though collimator and mask must be compatible to avoid systematic noise.

The reconstruction method will deal with the design properties.

1.3 Methods of Reconstruction (JG)

Several reconstruction processes, deconvolutions and correlations, have been proposed for coded mask cameras.

The algorithms can almost be chosen arbitrarily. While the aim of the reconstruction and the pattern of the mask partly decides the reconstruction algorithm, thus different algorithms have various advantages[8][16].

Some simple math can describe the basics of reconstruction. Any flux tributes to the shadowgram, denoted J. The source flux, S, and the diffuse background, D, are modulated by the mask elements, M, a matrix with 1 for transparent mask elements and 0 for opaque mask elements. The instrument background or signal-independent noise, B, is not modulated by the mask. We obtain the coding-equation with the correlation operator $\star$ as:

$$J = (S + D) \star M + B \tag{1.1}$$

In order to obtain the reconstructed image, $\widehat{S}$, or the original sky image,$(S+B)$, the shadowgram must be correlated with a decoding function or matrix, G, so:

$$\widehat{S} = (S+D) \star [M \star G] + B \star G \tag{1.2}$$

[4][16][8]

To obtain a δ-function, through the correlation, it is obvious that $\widehat{S} = (S+B)$is needed. The described reconstruction is normally referred to as the *direct deconvolution*, however due to noise (background, statistical noise etc.) this linear method is rarely usable to obtain good results.

1.3.1 Cross correlation

The most common method of image reconstruction may be the Cross Correlation, that is applied to an ideal detector (low noise, no systematic noise etc.), which in most situations is not the case. However it gives a good first hand estimate of the reconstructed image, and the method can easily be expanded with several of the below described "better" methods of image reconstruction.

During the cross correlation, $\otimes$, we wishes to obtain that the reconstructed sky equals the detected sky through a correlation between the recorded image and the reconstruction matrix (G with elements g_l^k):

$$\widehat{S} \equiv J \otimes M = (S+D) \tag{1.3}$$

Cross correlation will for a sky element k give

$$\widehat{s}_k = b \sum_{l \in J^k} g_l^k + \sum_i s_{p(i)} \sum_{l \in J^k} c_l^{p(i)} g_l^k \tag{1.4}$$

where $c_l^{p(i)}$ is a mask element (0 for opaque and 1 for transparent) mapped by a point source i, in the sky elements $p(i)$, on a detector element with intensity $s_{p(i)}$, and b is the background.

For a point source in sky element $k = p(i)$, one obtains that
$\sum_{l \in J^k} c_l^{p(i)} g_l^k = \begin{cases} n^k[o] \\ n^k[c] \end{cases}$ is the number of transparent [o] respectively opaque [c] mask elements.

The result is $\widehat{s}[o]$ containing the source and background counts and $\widehat{s}[c]$ containing background and the sources correlated with the mask, which in fact is noise.

By normalizing with the number of mask elements respectively, and subtracting the opaque elements from the transparent elements, the background is subtracted.

Ideally there are no noise, so $\widehat{s}_k = s_k$ [8]. This also implies that the background is uniform and perfectly subtracted. This is though never the case, thus there may be reason to use one or more of the below described correlation methods to obtain even better results.

1.3.2 Other linear reconstruction methods

Some other correlation methods are based on the linear reconstruction ideas of the Cross Correlation. *Finely Sampled Balanced Correlation*, evolved from *Balanced Correlation* are such excamples.

Instead of using 1 and 0 for transparent and opaque mask elements in the reconstruction matrix G, an opaque element is represented by -1. The Finely Sampled Correlation Method substitutes all these with n $\times$ n matrices of 1 respectively -1 to achieve more accuracy.

Also the *Delta Decoding* uses 1 and -1 to represent the mask elements. But instead of substituting with n $\times$ n matrices of 1 respectively -1, only one 1 or -1 is represented in each matrix, all other values are 0. Thus the reconstructed image is less blured.

1.3.3 Photon tagging

By tracing any photons i a specific area (of the detector) from a detection through any possible transparent mask element, the photon will be added as a source event, at that position of the sky. If the photon fails to be traced through any transparent element, the photon will be added to the background.

This offers the posibility of analysing a source without deconvolute the shadowgram first, thus the background contribution can be subtracted directly.

It is then possible to achieve good time and energy estimates of a source in a fast way.

The process is superior to the Cross Correlation for small numbers of photons, or if only a small part of the shadowgram is analyzed, e.g. if a source position is already known[5].

Further effort in the Photon tagging has resulted in *Maximum Likelihood Method*[11], a generalization, which takes effect form aperture, like imerfections of the detector, the support structures ect. into account.

The method rates the probability, that the intensities of the located sources will yield the observed shadowgram. The maximum likelihood of the combination of source intensities creating a similar shadowgram, is the solution to the algorithm.

The method is fast to produce more details, once sources are known, and it will reduce errors in spectra and other artifacts. It may be usefull for extracting better informations on a specific source.

1.3.4 Wiener filtering

For reduction of coding noise, due to dead detector regions and effects from imperfect coding, Wiener filtering may be regarded as a weighted cross correlation.

Wiener filtering are rarely used because of the use ideal (creating no artifacts) mask patterns (URA), that have no or little coding noise. However it may come to use due to its ability to reconstruct a damaged image.

Newly Rideout and Skinner[9] improved Wiener filtering as a generalisation in *minimum-mean-square-error* (MMSE). Though this method is very computationally demanding.

1.3.5 Iterative reconstruction methods

Iterative reconstruction methods is yet another way of correlate and improve the image.

Iterative Removal of Sources (IROS)

In order to avoid coding noise arisen from the cross correlation, iterative removal of sources work as an extension of the cross correlation.

After a cross correlation, point sources are extracted from the image. A simulation of these point sources are subtracted from the image. And thereby coding noise will become smaller than statistical noise, and intensities and positions for point sources can be better determined.

After iterations the sources are added back into the image again.

Maximum Entropy Method (MEM)

Data from corrupted or damaged cameras may be difficult to handle by linear reconstruction methods, due to increased noise, incompleteness and systematic and non-systematic errors. MEM offers a way of constructing the image despite lack of informations.

Maximum entropy method makes a new image from each iteration. Through maximisation of an entropy function the method finds the image that is in the best accordance with the detected image.

E-M algorithm

E-M algorithm is a two step iterative reconstruction method. For each iteration the steps are, first making the Expectation value for a probability function and then Maximize the expectation value.

This method is less demanding of computer power than the other iterative methods, and still it produces good results.

1.4 Non-uniform background (JG)

Many of the above described reconstruction methods require an ideally detected image, i.e. the background, consisting of two elements, the diffuse X-ray background (described in chapter 4) and the cosmic radiation or particle background (discussed in chapter 5, is uniformly distributed throughout the detector plane. However this is seldom the situation at hand, and especially not for space-borne detectors[1] like time variations, spatial vriations, orbital parameters and sun influenced variations.

This often gives rise to various problems like high noise level and ghost sources (peaks in the image, which is not a real X-ray source).

Ghost sources are often results of imperfect reconstruction methods or imperfect aperature (i.e. mask, detector). Often this is a result of sources detected in the PCFOV which produces artifacts as coding noise[2] and is therefore often seen far off-axis.

Other ghost sources may be results of statistical noise, due to low SNR. SNR may be improved through longer exposures, and ghosts will thus disappear.

In fact any irregularity in the background give rise to ghost sources[12].

There are two main groups of methods to resolve the problem of non-uniform background (except for the latter described reconstruction methods that takes the background into account). Those that removes the background and those that straightens out the background or smoothes the image.

1.4.1 Removal of background

In the assumption that the background is approximately constant in time, normalized blank field images may be subtracted from an observed shadowgram. This method requires blank field exposures, observations of sky regions without sources. And enough to avoid statistical fluctuations in the blank field. Othervise one may attemp to simulate the background, and then subtract it.

1.4.2 Smoothing of image

As a method of smoothing the image, one could use a low-pass filter. Through folding with, e.g. a gaussian function with proper chosen σ, one obtains that large structures in the shadowgram is (largely) removed, and hence not sources because of their small spatial extent, and therefore most ghosts arisen from coding noise will be removed as well.

If σ is chosen too small the low-pass filter will remove the sources as well, on the other hand too large σ will not remove the ghost sources.

Fluctuations as a result of statistical noise, e.g. Poisson distributed noise, will remain after such a filter, and still produce ghost sources.

Iterative image reconstruction methods, like IROS and MEM (previously described), offers the methods to override the statistical noise problem.

Chapter 2

The INTEGRAL mission and JEM-X

2.1 The INTEGRAL satellite (JH)

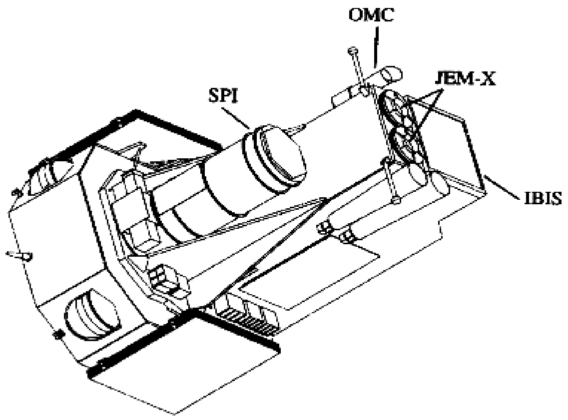

Figure 2.1: INTEGRAL

The International Gamma-Ray Astrophysics Laboratory (INTEGRAL) is selected by ESA to be the next medium-size scientific mission (M2) to be launched in September 2001. The mission of INTEGRAL is to provide the scientific community with an unprecedented combination of imaging and spectroscopy over a wide range of X-ray and gamma-ray energies including optical monitoring [15].

The INTEGRAL mission consists of four instruments:

- SPI: The spectrometer, designed to perform fine spectroscopy of narrow lines in the energy range 20 keV - 8 MeV.
- IBIS: The imager, designed to perform accurate point source imaging and broad line spectroscopy in the energy range 15 keV - 10 MeV.
- OMC: The optical monitor, designed to perform optical monitoring of high energy sources in the wavelength interval 500 - 850 nm.
- JEM-X: The X-ray monitor, designed to perform source identification and monitoring at X-rays wavelengths in the energy range 3 - 35 keV.

In the following JEM-X will be described in detail.

2.2 JEM-X (JH)

JEM-X (Joined European Monitor of X-rays) is designed to extend the energy range covered by the gamma-ray instruments (IBIS, the onboard imager and SPI, spectrometer), from their thresholds of 20 to 30 keV downward to about 3 keV. Furthermore JEM-X will provide more accurate positioning of new X-ray sources than available from the other instruments. The JEM-X is designed and built by a consortium of six European laboratories with The Danish Space Research Institute (DSRI) as the principal investigator institute.

The monitor actually consists of two identical, coaligned coded mask telescopes, with differently oriented masks, to minimize systematic effects. The coded mask telescope basically consists of three major parts, the coded mask, the collimator and the detector [7].

2.2.1 The Coded Masks

The coded masks are made from 0.5 mm tungsten. Each mask consists of approximately 23500 hexagonally shaped cells. Of these, approximately 5900 are open, giving ≈25 % open area. Each cell has a size of 3.3 mm, giving the mask a total diameter of 535 mm. To support this relatively thin structure, there is a mask suspension structure placed on both sides of the mask enabling it to withstand the launch stresses [7].

The pattern for the mask is a Hexagonal Uniformly Redundant Array (HURA), based on a Biquadratic Residue Set, constructed from the prime number 22501, that is rotated 120 degrees, thus repeating itself.

The mask, including the suspension structure, are shown on the front page.

2.2.2 The Collimators

The collimators limit the Field Of View (FOV) besides supporting the thin detector windows. The collimator has a square design, which has been proved to be compatible with the hexagonal masks, with a inside width of 6.6 mm and a height of 57 mm. These dimensions cut off the input to the detector at 6.6^o off-axis angle to maximize the signal to noise ratio. The collimators are basically made of 180 μm molybdenum. But the K-fluorescence photons produced by the molybdenium could contribute to the detector background, so the molybdenum is covered on both sides with 35 μm copper to reduce this contribution. Finally the copper is covered with a 100 μm aluminium layer to absorb the 9 keV K-fluorescence photons of copper. Thus the total thickness of the collimator walls becomes 0.45 mm [7].

2.2.3 The Detectors

Below the collimators or 3.4 meters below the coded masks the detectors are located. The detectors onboard JEM-X are of the type *high pressure microstrip proportional gas chambers* [7]. This detectortype is basically a chamber filled with gas under high pressure, in this case the gas is a mixture of 90% xenon and 10% methane under a pressure of 5 bar. When a X-ray hits the detector window and enters the gas it travels a certain length before interacting with an atom in the gas, removing an electron from the atom. The electron hits more gas atoms and a small cloud of electrons is created. The electrons hit the anode, located 55 mm below the window, giving rise to an electric pulse, proportional to the number of electrons in the electron cloud. This number is proportional to the energy of the original X-ray photon and therefore, the size of the pulse also reveals the energy of the original X-ray photon. The detectors for JEM-X are designed to detect X-rays in the energy range 3 - 35 keV, but the dectection can be extended up to 60 keV [7]. The electrodes are so-called microstrips with alternating anode (8-12 μm) and cathode strips (455 μm) on a 1.055 mm pitch, on a glass plate[1]. This gives one co-ordinate of the event position. The other co-ordinate is obtained from perpendicular electrodes on the other side of the microstripplate. This setup gives a position resolution better than 1 mm for on axis events, corresponding to a basic angular resolution of 3'. Raytracing simulations have verified, that this resolution can be achieved. Below the microstrip plates is located the detector electronics, which provides the neccesary preamplification of the anodes and cathodes. The whole detector setup, microstrip plates and electronics are encapsulated in panshaped detector box made of 2 mm stainless steel, to minimize weight and maximize strength [10].

The detector windows are 250 mm in diameter (thus giving each unit a detector area of 500 cm^2), and are made of 250 μm beryllium foils, supported by the collimator structures. This size and position of the detectors relative to the masks gives a Fully Illuminated Field Of View (FIFOV) of 4.8^o (in diameter) and cuts off the field of view at 6.6^o off-axis, i.e. the same angle for which the collimators have zero transmission [7], [10]. The dectorbox, including the collimator, are shown on the front page.

2.3 The onboard computer (JH)

The main purpose of the computer onboard INTEGRAL is to receive the data from the various instruments and transmit the data to Earth. INTEGRAL has a rather traditional communication module, which means that there are restrictions on the data transmission rate. Because of this the telemetry rate from both JEM-X units is restricted to 6.7 kbit s^{-1}. In the basic mode where the maximum amount of details of each event are transmitted, each event take up 32 bits, this implies that the counting rate cannot exceed approximately 100 counts s^{-1} per JEM-X unit, without loss of data, corresponding to a 500 mCrab source. In conditions where the sources exceed this strength a grey filter can be applied, where only a fraction of the events are transmitted. Several other modes for extracting specific information are available, e.g. a spectrometer mode, where position information is disregarded [13]. The JEM-X units can be assigned different modes, so that e.g. one unit can function as a spectrometer and the other as an imaging device.

The onboard computer also has the possibility to reject events. This is especially important in relation to the cosmic radiation background, where the computer is able to reject a large amount of the incoming radiation by analysing the eventinformations. E.g. if a event deposits energy several places in the detector at the same time, it is assumed to be due to a particle and by analysing the pulse shape and pulse height, events can also be rejected. It is estimated that this will be able to reject as much as 99 % of the events that originates from the cosmic radiation [12].

Table 1 below summarizes the characteristics of JEM-X [15].

[1] A Schott-8900 substrate

1 **Table 1**	**JEM-X**
Energy range	3 keV - 35 (100) keV
Detector area (cm^2)	1000 (2 units each 500 cm^2)
Spectral resolution ΔE/E (%)	$47/\sqrt{(E/1\text{ keV})}$
Field of view (fully coded)	4.8^o
Angular resolution	3' FWHM
Typical source location	< 20 "
Continuum sensitivity (3σ, 10^6 s)	9×10^{-6} at 6 keV (ph cm^{-2} s^{-1} keV^{-1})
Line sensitivity (3σ, 10^6 s)	1.7×10^{-5} at 6 keV (ph cm^{-2} s^{-1} keV^{-1})
Timing accuracy (3σ)	10 μs
Mass (kg)	65
Power (W)	52
Data rate (kbps)	6.7

2.4 The mission scenario for the JEM-X (JG)

The INTEGRAL satellite will be launched using a Russian PROTON launcher to a high eccentric orbit with apogee at 115 000 km and perigee at 48 000 km with a period of 72 hours (alternatively with an ARIANE 5 launcher: apogee 117 000 km, perigee 4 000 km and a period of 48 hours). This high orbit places the satellite outside the denser regions of the electron radiation belt (approximately untill 16 000 km) which allows the satellite to be observing for almost 100 % of the time[15].

Particle radiation will be continously measured to minimize the problem of time variation dependence in the cosmic radiation risen from radiation belt passages and solar flares.

2.4.1 Observing the universe with INTEGRAL

The instruments onboard the INTEGRAL satellite are combined the most powerfull tool for strong X- and γ-ray radiation so far.

While SPI performs spectral analysis with narrow-line sensitivity of point sources in the gamma energy region, and IBIS is sensitive to continuum and broad line spectras and provides source identification in a broad gamma energy range, the OMC (monitoring the X- and γ-ray sources in the optical region) and JEM-X will observe both spectra and position for sources with radiation in the energy region of hard X-ray emmision.

This wide span in energy makes the INTEGRAL satellite exceptional for simultanously observations of high energy sources, both for time variations and for complete spectra in the whole energy region of the INTEGRAL.

With an angular resolution of 3' the JEM-X is good equipped for its primary goal: to detect and identify sources and observing, in co-ordination with the other INTEGRAL instruments, in the hard X-ray energy region, the lower part of most X-ray and γ-ray source spectre. Interesting for the JEM-X will be the 6.4 keV Fe line, which is possibly to identify in several X-ray source spectres.

Concretely, more sources are of interrest for JEM-X, with the center of the galaxy as the perhaps most exciting known group of sources. With several strong sources within a few degrees, with hard X-ray radiation, this region of the sky is the densest known place in the sky with separated X-ray sources.

Other objects of interest for JEM-X are such as:

- Compact objects, especially Black Hole Candidates (BHC). These structures seems to be highly active in the X-ray region of the spectra for JEM-X. In this category spectras and time-variations of binary systems with X-ray pulsars, having strong magnetic fields, could through observations establish better knowledge of late star evolution. Several of the binaries appears to be BHC, which is expected because of their particularly hard spectra (energy region 50 - 100 keV). However to establish whether they truly are Black Holes, further observations will be nescesary and possibly by INTEGRAL.

- Galactic structures: clouds, interstellar medium, cosmic radiation distribution and mapping of continuum and line emission.
- Extragalactic Astronomy: clusters, active galactic nuclei (AGN), cosmic diffuse background. The time-variations has only been simultanously observed for a few AGN, and the energy cut off has only been determined for one[13]. In later theory the Diffuse X-ray Background is thought to be emitted from outnumberous distant and fainth AGN, especiallythe subtype Seyfert galaxies. With INTEGRAL it will be possibly to make simultaneously X- and γ-spectra of several extragalactic objects.
- Stellar Nucleosynthesis: Hydrostatic Processes, Supernovae and Novae.
- High Energy Transient, Particle Prosesses and Acceleration, Transrelativistic Pair Plasmas.

Hopefully the observations will also find unidentified X- and γ-ray sources and other unexpected discorveries.

2.4.2 The observing programme

The nominal mission life is 2 years with an extended mission life up to 5 years. Observations will mostly last from tens of minutes till two weeks.

Observations will be split into two parts:

- The Core Programme (approximately 1/4 to 1/3 of the observation time) is the guaranteed time for scientist, institutes and others who had made contribution to the programme. This time will be used for a Galactic Plane Survey and pointed observations of selected regions.

  By stepping a few degrees between each exposure, with a few to tens of minutes per exposure, the Glactic Plane Survey will map emission in the galactic plane, and hopefully detect new sources as well.

  The pointed observations is yet to be determined by the members ofi the INTEGRAL Science Working Team. ["INTEGRAL: the international gamma-ray astrophysics laboratory" Christopher Winkler]

- The General Programme, the remaining time, which will be awarded to the scientific community. Observation proposals will be selected by a Time Allocation Committee and called for from one year before launch.

Chapter 3

JEM-X software (JH)

The JEM-X simulation software package, is the primary tool we have used to perform our analyses. This is a software package, developed at DSRI, which enables a complete simulation of a single JEM-X unit, from the simulation of X-ray sources in the sky to registration of X-ray photons in the detector to the image reconstruction. In the following we explains the different steps involved in making a simulation run.

3.1 Simulation of X-ray point sources (JH)

First one must define the X-ray sources that will be used in the simulation. This is done by writing the desired source characteristics to a text file (one line per desired source) that are used as input to the program. The primary input parameters[1] are:

- The position of the source. The coordinates of the source is given in coordinates as seen from the satellite in arcminutes.
- The spectral type of the source. We have in our simulations assumed that the spectrum is given by a power law, other spectral types are possible, for instance a black body or thermal bremsstrahlung spectre.
- The source strength. This is the primary source parameter which we have varied in our simulations as explained in the following chapters. The source strength is given in units of erg cm^{-2} s^{-1} integrated over the energy interval 2 - 10 keV. This notation is used throughout the report.

Using these parameters the program then calculates all the photons that hit the satellite and generates a photon file in the FITS[2] format, with information on all the photons that hit JEM-X originating from the simulated source(s).

3.2 Simulation of background radiation (JH)

In addition the radiation originating from X-ray point sources, there is two other major contributions to the radiation field; a) the diffuse X-ray background and b) the particle induced background.

[1]Other parameter can be set,e.g. the column density of hydrogen atoms from the souce to the satellite, but these are of not of importance to our project.

[2]FITS - Flexible Image Transport System. A widely used data file format which allows many data to be efficiently stored in a single file.

3.2.1 The diffuse X-ray background (DXB)

The diffuse extra-galactic X-ray background is assumed uniform on the sky and constant in time. Calculation of the contribution from the DXB is included in the software package and is added to the radiation originating from the individual point sources. In our simulations the DXB is defined as $I(E) = 11.0 \cdot E^{-1.46}$ photons cm^{-2} s^{-1}keV^{-1}sr^{-1} in the energy range 1 keV $<$ E $<$ 60 keV. The DXB is further described in chapter 4, [14], [12].

3.2.2 The particle induced background (PBG)

The particle induced background consists of highly energized particles and gamma photons that hit the satellite and give rise to detector counts, primarily via interaction with the matter in the satellite, producing secondary radiation. But the distribution of this radiation in the detector has been showed to be non-uniform [6], [8]. To include the effects of a structured PBG a FITS file is given as input, describing the distribution probability of this radiation in the detector, so that it is possible to simulate e.g. an enlarged PBG radiation level near the edge of the detector [14].

3.3 The raytracing (JH)

When the photons from the point sources and the DXB have been calculated, every photon hitting the mask of JEM-X is raytraced through the satellite, calculating whether it hits an open or closed mask element, taking into account absorption probabilities when it hits matter. Finally the position in the detector gas, the detection depth and the detected energy of the photon is calculated and all the data relating to the photon is recorded in a new FITS file, the event file. When all the photons from sources and the DXB have been raytraced through the satellite structures, the PBG contribution is added to the event file.

The event file thus is a list of all the photons recorded in the detector, with extensive information on each photon, e.g. the orginal energy of the photon, the detected energy of the photon, the detection depth in the gas etc. This information is used to construct a shadowgram, that is, the image that all the combined contributions produce in the detector [14].

3.4 Image reconstruction (JH)

In order to complete the simulation, the skyimage needs to be reconstructed as explained in chapter 1. The simulation software uses the simplest type of reconstruction, namely that of cross correlation. When the reconstruction is complete an image of the sky, as it is expected to be seen from the satellite, is produced. This process completes the simulation run [14].

The whole simulation process has been implemented in a perl script, which makes the simulation process semiautomatic.

3.5 Other tools (JH)

In order to analyze the image we have also used a number of other programs. Most of these are written by us and represent a significant amount of programming time.

find_sources.pro[3] is a IDL program, which searches the final image for sources. The user specifies what detection level[4] the program should use as a criterion as to whether or not a peak is accepted as a source. The details of the found sources is then put in a file for later

[3] Written by N. J. Westergaard

[4] The detection level is defined as the peak size diveded by the local rms (excluding the peak) surrounding the peak.

inspection and possibel comparison with the input source file to determine if the peaks found by *find_sources* are sources or ghosts. After conferring with N.J. Westergaard, we decided to use detection level = 10 as the threshold for accepting peaks as sources.

compare.pro (JH) is a small IDL program which compares the positions of sources in an reconstructed image with the positions of the input sources to determine whether or not a found peak is caused by a "real" source. A small displacement is accepted, since the the detected photon travels a certain length in the gas, before being detected. This means, that the positions of the sources are displaced in a systematic way. We have allowed a displacement of 6 srcminutes. However, the average displacement is expected to be a function of the incident angle.

distribution.pro (JH) is an IDL program that takes a FITS image file and displays the number of counts in sectors of equal area e.g. 6 annulars of equal area. Due to the square shape of pixels, selection effects occur so that sectors of equal area, does not have the same number of pixels. The program corrects for this effect by carefully normalizing the number of pixels in each sector.

reduce_bkg.pro (JH) is a IDL program that applies a low-pass filter to a shadowgram by convolving it with a gausssian with σ =4 pixels. This σ was chosen, because this scale is larger then the peaks in the shadowgram that is caused by point sources, but smaller then the bacground structures, hence the peaks will not be seen by the convolving function. Before the shadowgram is convolved the outer 20% of the shadowgram is enlarged and placed as an annular around the shadowgram, thus making it larger. This is done to avoid edge effect in the convolved image. Finally the convolved, or filtered image, is subtracted from the original shadowgram, creating a new shadowgram with a reduced background. This image is refered to as the smoothed image in the text.

ghostbuster.perl (JH) This is a perl script, which automates the whole simulation process, i.e. running the actual simulation, finding sources, convolving the shadowgram, finding sources in the shadowgram and comparing the found sources with the input sources. The is a rather timeconsuming proces, because of the large number of required computations, a single simulation run takes several hours to complete.

Finally we have also found the *ftools* package very useful in investigating and manipulating the produced FITS files. This is a software package designed to manipulate and extract data from FITS files.

Chapter 4

The diffuse X-ray background (JH)

The diffuse X-ray background (DXB) is one of the two major contributions that affects the shadowgram, not coming from detectable sources (the other, the particle induced radiation background is explained and analyzed in chapter 5). The DXB is due to unresolved sources (mainly extra-galactic) and thermal galactic emission in the energy range where the detector is sensitive. The DXB hits the satellite and the mask like radiation from other X-ray sources and therefore it is a coded image of the DXB that is seen in the shadowgram. This implies that if one wants to accurately account for all the background contributions, a model of the DXB must be subtracted from the reconstructed image. However, because the DXB is assumed to be uniform and constant in time, the effect on the shadowgram is assumed to be constant and therefore the DXB can be subtracted from the shadowgram before the image is reconstructed [6].

In this chapter we analyse the spatial distribution of the DXB in the detector.

4.1 Assumptions / The modeling (JH)

The simulation software assumes that the DXB is evenly distributed across the sky with a spectrum according to the power law $I(E) = 11.0 \cdot E^{-1.46}$ photons cm^{-2} s^{-1}keV^{-1}sr^{-1}in the energy range 1 keV $<$ E $<$ 60 keV. From this we expected a centrally peaked distribution with no azimuthal dependence [12], [2].

4.2 The distribution in the detector (JH)

We wanted to analyze the distribution the DXB contribution has in the shadowgram and especially determing, whether or not the DXB can be approximated by a flat distribution. We did this by simulating a very long exposure (50000 s) and subtracted all other radiation, so that we had an image containing only the DXB contribution which had hit the detector, this was equal to 407410 photons or a countrate of approximately 8 counts/s. To analyze the distribution, we divided the detector into different areas, namely 12 slices of 30 degrees each (to investigate the azimuthal distribution) and 6 annulars of equal area out from the center of the detector (to investigate the radial distribution).

4.2.1 The azimuthal distribution

First we examined the azimuthal distribution. The number of counts in each section is plotted figure 4.1 in the left half of figure. The errorbars in this plot is calculated as $\sqrt{N}$, where N is the number of counts in each section, according to Poisson statistics, which is applicable to photon distributions. We expected to see a flat straight line, meaning that the detector receives a equal number of counts in all directions, because the DXB comes equally from all parts of the sky.

When testing against this hypothesis the reduced χ^2 is 1.02 that is, it can be justified that the distribution, within the errors, has no azimuthal variation.

4.2.2 The radial distribution

Next we examined the radial distribution of the DXB. This was done by dividing the detector plane into 6 annulars of equal area, from the center and out, and then plotting the number of counts from the DXB in each section, after appropriate correction. This plot is shown in the right half of figure 4.1, errorbars calculated as described above. This plot shows a statistically very significant centrally peaked distribution. There is approximately an 15 % difference between the number of DXB counts from the center section and the edge annular.

The reason for the peaked distribution must be sought in the complex relationship between the size of the mask and the distance to and shape of the collimator.

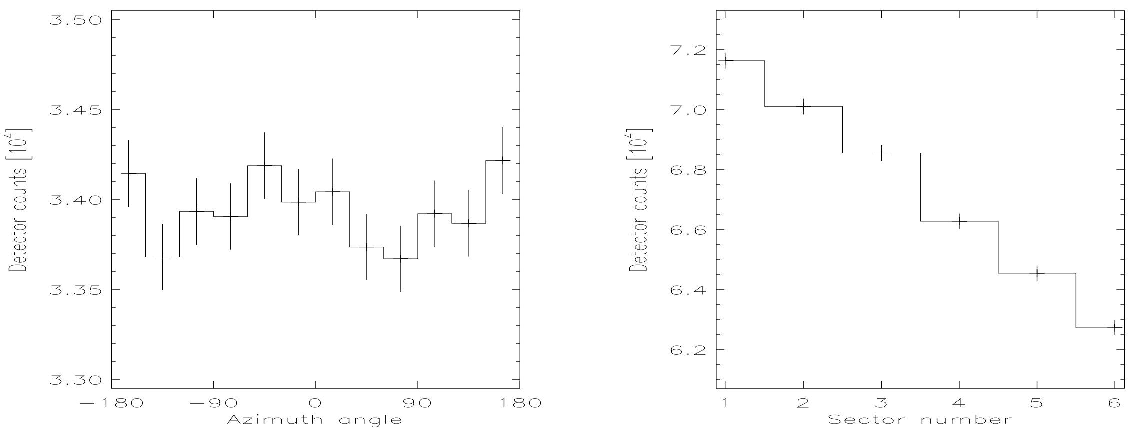

Figure 4.1: The DXB distribution.*Left:*Azimuthal distribution of DXB. *Right:*Radial distribution of DXB in annulars of equal area from detector center (sector 1) to detector edge (sector 6). Errorbars is $\sqrt{(\text{counts})}$

Chapter 5

The cosmic radiation background

5.1 The background problem (JH)

The INTEGRAL satellite will be launched into a high-Earth type orbit. This implies that the satellite will experience an unshielded cosmic radiation field. The cosmic radiation field (CR) consists of galactic cosmic rays and energetic charged particles from the Sun. When the CR hits the satellite it give rise to detector counts by one of three mechanisms[6]:

a) direct interaction of the CR with the active gas

b) secondary particles produced by the interactions of the CR with the satellite structures

c) activitation of the satellite detector, generating delayed radioactivity.

Although the onboard computer is able to reject most detector counts originating from the CR (see section 2.3), a fraction ($\sim$ 1% or less [12]) of the CR induced counts, will still be accepted as X-ray photons. This makes the CR a possible source of error, because it will give rise to an enlarged (probably non-uniform) particle induced background (PBG).

We have tried to analyze what effects the PBG may have on the results, by simulating various background distributions and comparing their influence on the results. Furthermore we have applied a low-pass filter to the different background distributions, to find possible advantages and disadvantages there may be in applying this technique.

5.2 A model of the estimated PBG (JH)

M. Feroci has via simulations shown, that contribution b) in the preceding section is the primary contribution to the PBG [6].

It is expected that there will be increased radiation levels from the parts of the satellite, which has mass concentrations, e.g. the other instruments. This is because that although mass concentrations are good radiation shields for low energy photons, they are at the same time good converters for high energy photons and particles [6].

The TIMM (The INTEGRAL Mass Model) working group, has computed the estimated PBG by transporting the CR through the satellite structures, counting the particles that interacts with the gas [6]. The results of this simulation is shown in figure 5.2. This figures shows the number of PBG counts, in selected regions of the detector, similar to the analysis in chapter 4.

The estimated PBG is clearly anisotropic distributed, both azimuthally and radially. The radial distribution shows an approximately 25% increase in the outer three sectors of the detector. This distribution corresponds well with experienced backgrounds from other X-ray missions that are flying (SIGMA, [2]) or have flown (EXITE, [1]), with an enlarged radiation level near the edge of the detector. Correspondingly there is an azimuthal distributed anisotropy, with an approximately 50% increase in radiation levels in the directions of the other instruments (SPI and IBIS) and the other JEM-X unit. This distribution is not surprising, since it shows enlarged radiation levels in the direction of the mass concentrations.

Based on figure 5.1 we have tried make a model of the estimated PBG. We constructed a model of the PBG distribution in the detector and simulated an observation from which we extracted the photons originating from the CR. The distribution of these was visualized in a way comparable with figure 5.1. This proces was repeated until we had a satisfying correspondence between the figures. The distribution from our PBG model is shown in figure 5.2. The left part of figure 5.11 shows the model we used as input to the simulation (see section 3.2.2).

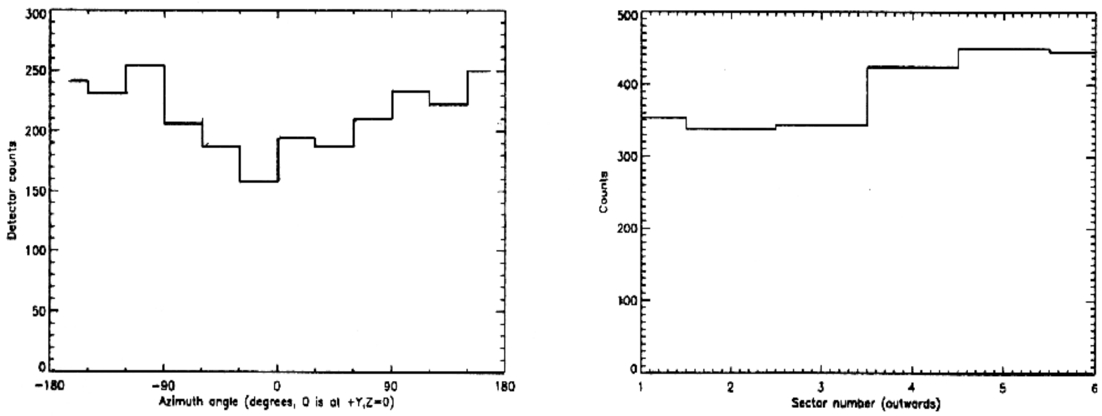

Figure 5.1: Distribution of the expected distribution background counts in the detector, from the CR input source. *Left:*azimuthal distribution of PBG. *Right:*radial distribution of PBG in annulars of equal area from detector center (sector 1) to detector edge (sector 6). Extracted from [6]

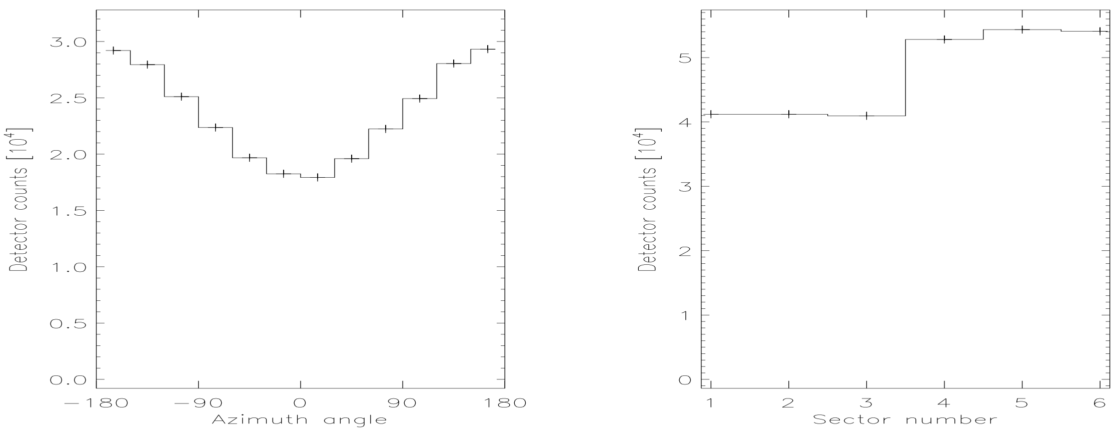

Figure 5.2: The PBG distribution from our model. See fig. 5.1 for caption. Errorbars is $\sqrt{(\text{counts})}$. Total nr. of PBG photons is 284579.

5.3 The PBG analysis (JH)

Using the model above, we wanted to analyse the effects the estimated PBG distribution would have on the imaging.

We did this by simulating observations similar to what is proposed. Four sources that were randomly positioned at a distance of 2 arcminutes from the center of the detector, were simulated. The sources were randomly placed in order to remove any effects caused by the position of the sources relative to the square collimator cells, see section 2.2.2. The four sources were simulated to be observed for 1200 seconds. This is similar to present observation scenarios, where the satellite in its dithering mode, will move in a pattern of points separated by 2 arcminutes, observing each point for approximately 20 minutes [15]. A small IDL program automated the generation of the randomly positioned sources. The part of the shadowgram that was formed by X-ray photons in the energy interval 3 - 20 keV, was then reconstructed. This energy range is adequate for the spectra of most sources [7]. Furthermore, this is the energy range where JEM-X is the only instrument onboard that is active.

The reconstructed image was then searched for sources by the IDL program *find_sources.pro* with a detection level threshold of 10 (see section 3.5) and the positions of the found sources were compared to the position of the original input sources. If the positions were sufficiently close to the input sources, the found sources was marked as positively identified sources, if not the found sources was marked as ghosts. This simulation was performed 25 times for each source strength and this was again done for source strengths in the interval $0.7 \cdot 10^{-10}$ to $2.0 \cdot 10^{-10}$ erg cm^{-2} s^{-1} in intervals of $0.1 \cdot 10^{-10}$ erg cm^{-2} s^{-1}.

The shadowgram was low-pass filtered by convolving the shadowgram with a 2d gaussian function with σ=4 pixels. The filtered image was subtracted from the original shadowgram, thus obtaining a shadowgram with a reduced background. This smoothed shadowgram was searched for sources as described above[1] (see section 3.5.

In the following, the results of this procedure are displayed and discussed for each of the three PBG distributions we have considered and their respective smoothed backgrounds.

5.4 The flat PBG (JH)

The flat PBG is the best thinkable, as a constant contribution is automatically subtracted in the reconstruction proces (Chaper 1), so that only counting and coding noise has an influence on the results. We therefore expected that this distribution would produce the minimum number of ghosts and the maximum number of detected sources that we would see in any PBG distribution, allowing us, by comparison, to determine the degree of error that a structured PBG would inflict.

The results of the simulations for the flat PBG is shown in figures 5.3 to 5.6. Figure 5.3 shows the average number of found and positively identified sources (left half) and ghosts (right half) for varying source strengths. Each point in the figure represents 25 simulations of four sources observed for 1200 seconds. The histograms behind each point shows the distribution of the identified sources and ghosts in the 25 simulations, in an effort to display the error in each point.

The left half of figure 5.3, shows that the average number of found sources is fairly constant for sources stronger then $1.3 \cdot 10^{-10}$ erg cm^{-2} s^{-1}. For these source strengths nearly 100 % of the sources have been identified in the reconstructed image. Simulations with sources weaker then $1.3 \cdot 10^{-10}$ erg cm^{-2} s^{-1}, shows a decrease in the number of identified sources, decreasing rapidly below $1.0 \cdot 10^{-10}$ erg cm^{-2} s^{-1}.

The right half of the figure shows that the average number of ghosts is nearly constant with an average of 0.9 found ghost per simulation. Small variations can be seen, but these are believed to arise from statistical fluctuations. No trend can be seen, implying that the average number of ghosts is independent of the strength of the actual sources that are observed.

In figure 5.5, the fully drawn line, shows the average detection level (see section 3.5) of the identified sources. The errorbars are calculated as RMS of the detection levels of the identified sources. The detection level seems to be an almost linearly decreasing function, expect for very weakest sources, where there is a tendency for the line to flatten. However, this is probably due to the detection threshold of 10 whereby sources weaker this threshold are removed, raiseing the

[1]The simulation run described above are somewhat timeconsuming. In its final form, a simulation run for a given PBG distribution takes approximately 36 hours to complete, not including to time spent to design a new PBG distribution or data analysis.

average detection level of the remaining sources. For the same reason the error bars in those three points are probably underestimated. This flattening can also be seen in figure 5.3, for the weakst source.

The fully drawn line in figure 5.6 shows the average detection level of the found ghosts, error bars as in fig. 5.5. The plot displays an almost constant detection level of approximately 11.

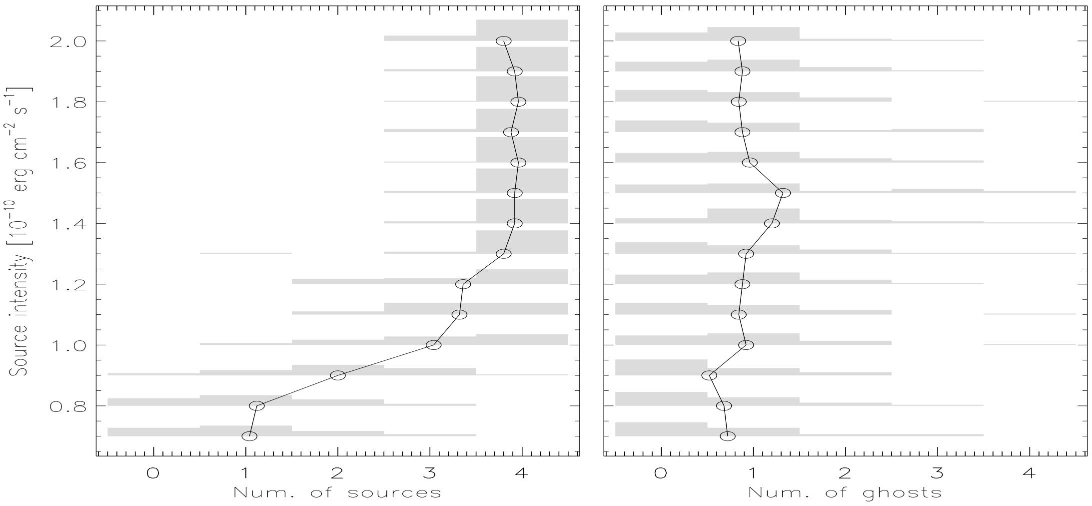

Figure 5.3: Average number of indentified sources (left) and ghosts (right) found in flat PBG. The histograms behind each point shows the distribution used to calculate each point.

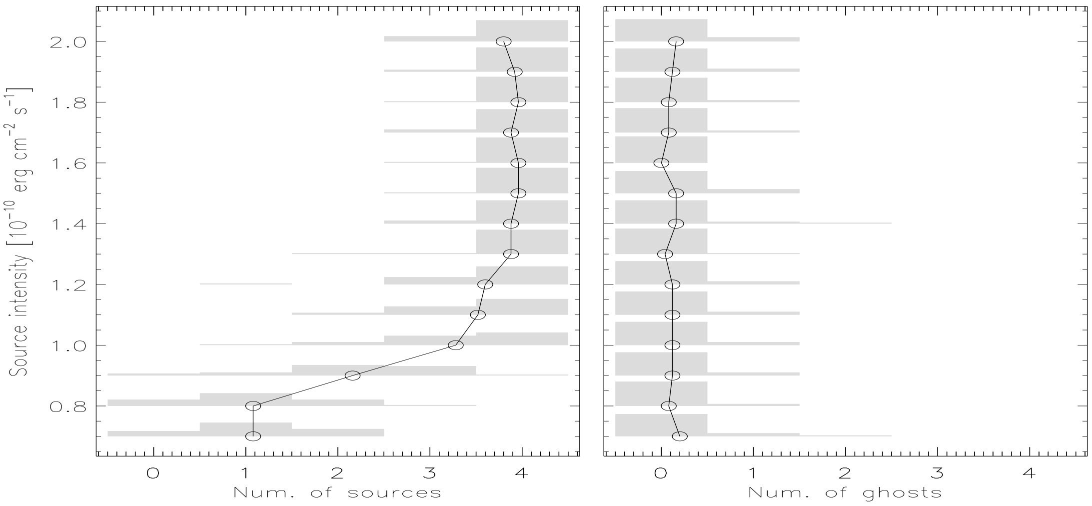

Figure 5.4: Average number of indentified sources (left) and ghosts (right) found in flat smoothed PBG.

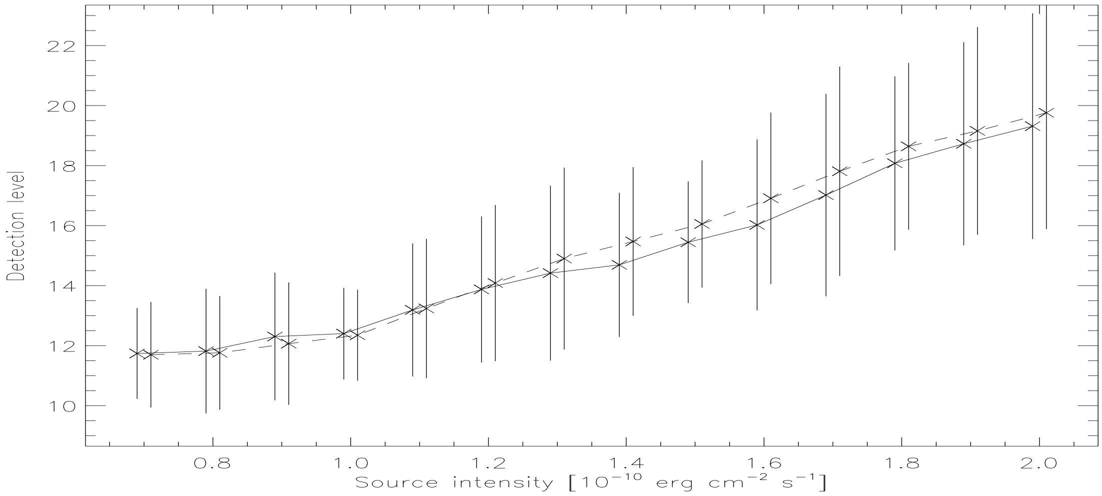

Figure 5.5: Average detection level of indentified soures. Fully drawn line:flat PBG. Dashed line:Smoothed flat PBG. Errorbars calculated as RMS.

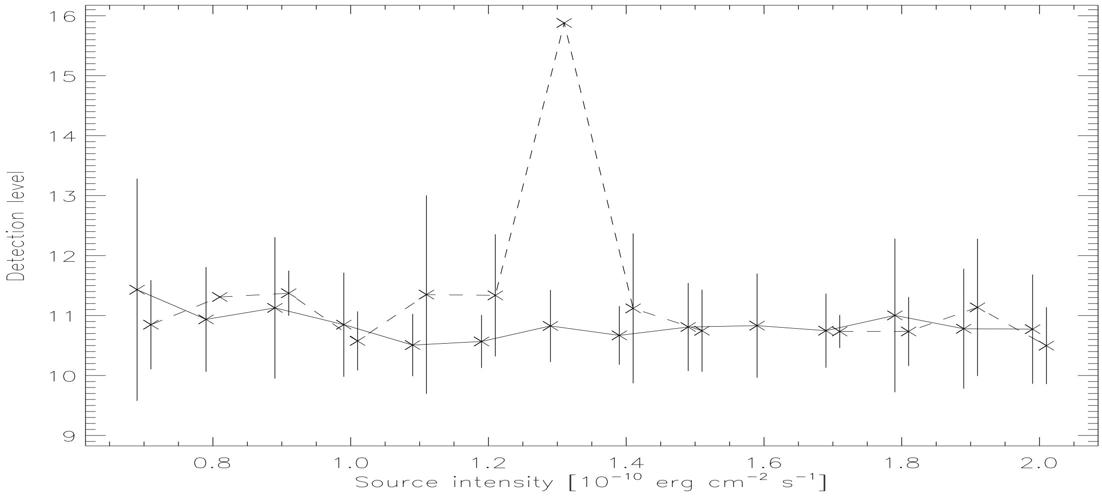

Figure 5.6: Average detection level of ghosts. Fully drawn line:flat PBG. Dashed line:Smoothed flat PBG. Errorbars calculated as RMS.

5.4.1 The smoothed flat PBG

Figure 5.4 shows the average number of identified sources and ghosts for the flat smoothed PBG. When the figures of the smoothed flat background are compared to the un-smoothed flat background it is seen that the number of identified sources is not significantly altered. In fact there seems to be a close correspondence. There may be a tendency for the smoothed background to detect slightly more sources, especially for weak sources, but the variations are within the estimated error. Thus the smoothing does not appear to have any significant effect on the number of found true sources. However, the smoothing has a very strong effect on the number of ghosts. The right half of figure 5.4 shows the average number of ghosts in the smoothed flat background. The figure shows that the average number of ghosts is significantly reduced from an average of 0.9 ghosts/simulation in the un-smoothed flat PBG to 0.1 ghost/simulation in the smoothed flat PBG.

The detection level of the found sources and ghosts in the smoothed background, is plotted as the dashed lines in figure 5.5 and figure 5.6 respectively. When the average detection level of the indentified sources is compared to that of the un-smoothed flat BPG (fully drawn line), a close correspondence is seen. The smoothed flat background have a tendency to have a little higher detection level of the indentified sources for sources stronger then $1.2 \cdot 10^{-10}$ erg cm^{-2} s^{-1} (which is the source strength from which the number of indentified souces is decreasing, see fig. 5.3 and fig. 5.4) , but the tendency is however still within the estimated error.

In fig. 5.6, the average detection level of ghosts in the smoothed flat background is also very similar to that of the un-smoothed flat background, and the smoothing appears to have a small effect on the average detection level, except for a single high peak at the source strength $1.3 \cdot 10^{-10}$ erg cm^{-2} s^{-1}. However, this peak represents only a single ghost (hence there is no errorbars) and it is hard to determine the significance of this peak. No point is plotted for the source strength $1.6 \cdot 10^{-10}$ erg cm^{-2} s^{-1}, because there were no ghosts present in these simulations.

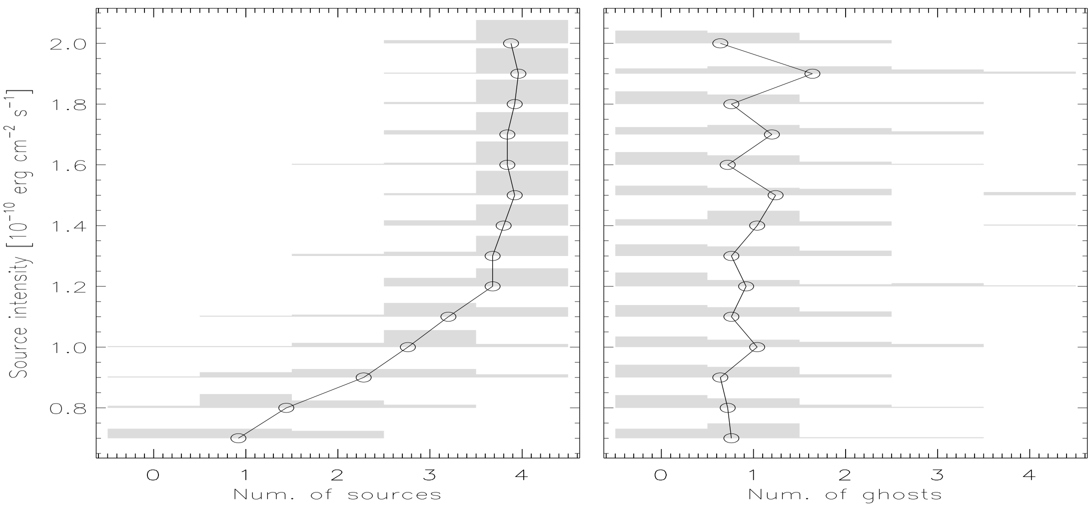

Figure 5.7: Average number of indentified sources (left) and ghosts (right) found in estimated PBG. The histograms behind each point shows the distribution used to calculate each point.

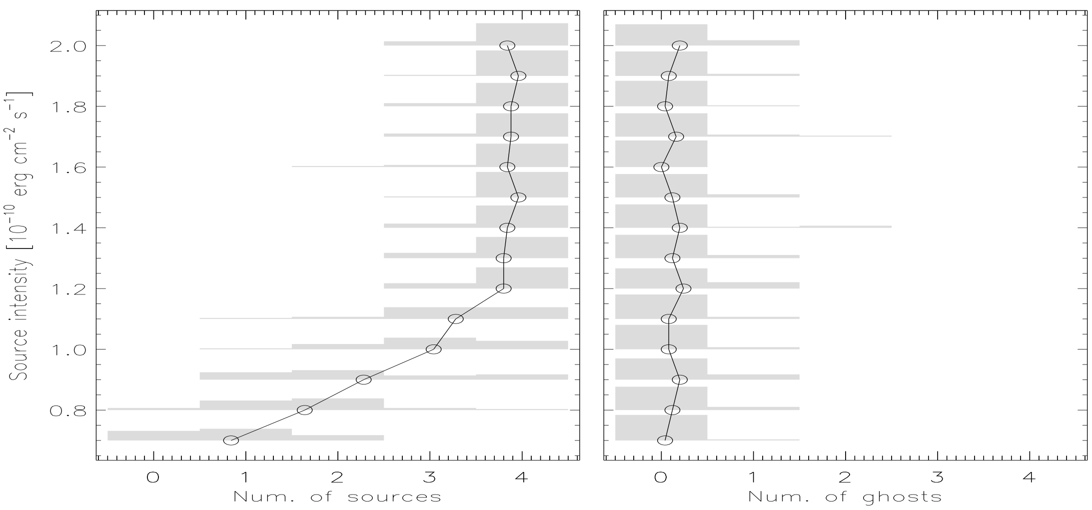

Figure 5.8: Average number of indentified sources (left) and ghosts (right) found in estimated smoothed PBG.

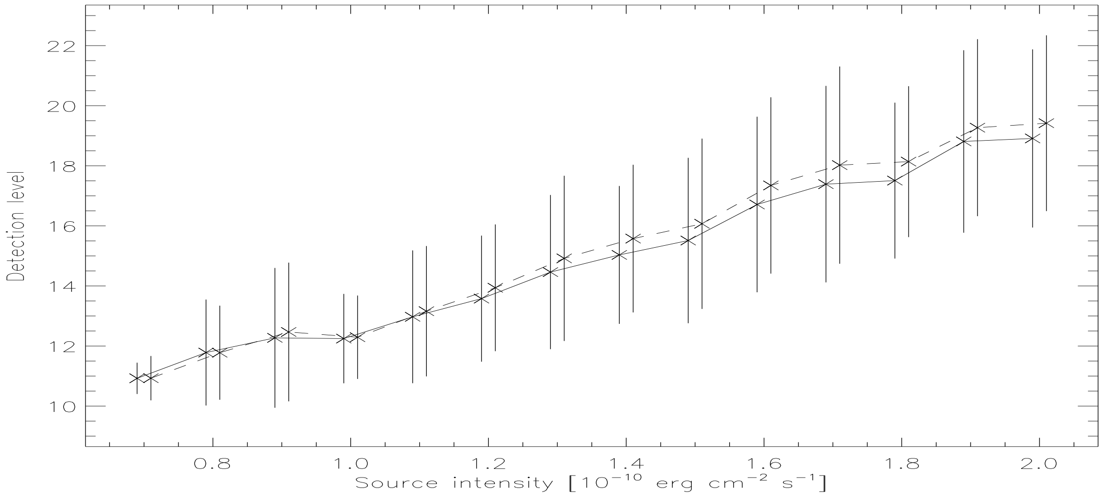

Figure 5.9: Average detection level of indentified soures. Fully drawn line:Estimated PBG. Dashed line:Smoothed estimated PBG. Errorbars calculated as RMS.

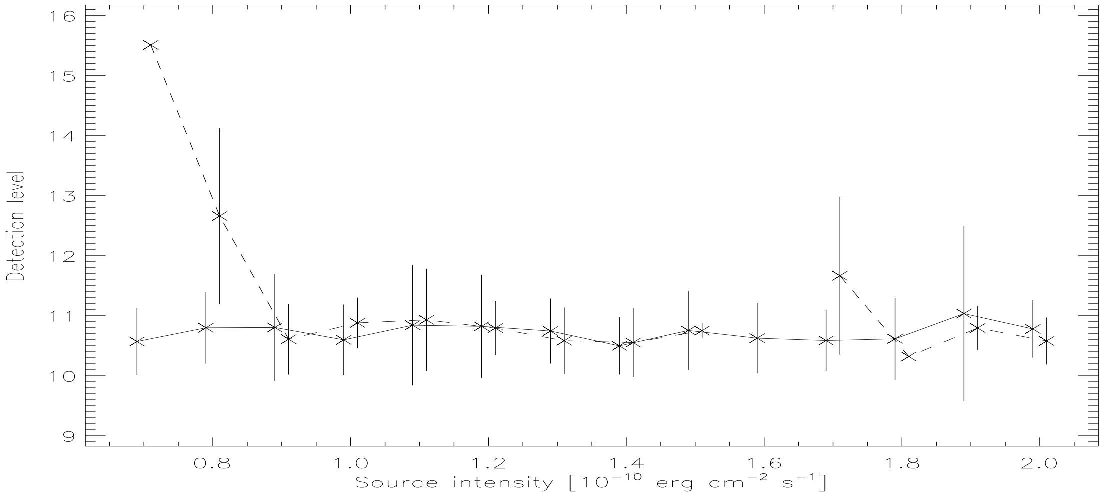

Figure 5.10: Average detection level of ghosts. Fully drawn line:Estimated PBG. Dashed line:Smoothed estimated PBG. Errorbars calculated as RMS.

5.5 The estimated PBG (JH)

We followed the same procedure as for the flat PBG to simulate the estimated PBG, using the model from section 5.2. Left half of figure 5.7 shows the average number of positively identified sources and right half shows the average number of ghosts in each simulation.

Figure 5.7 has the same structures as the flat background. For strong sources, the average number of identified sources are approximately constant at a high value, very close to a 100% detection rate. But when the source strengths falls below $1.3 \cdot 10^{-10}$ erg cm^{-2} s^{-1}, the graph decreases rapidly. There are minor differences, between the estimated PBG and the flat PBG (fig. 5.3) e.g. the point where the curve rapidly decreases, but it's hard to say whether this is just due to statistically fluctuations, at present our statistical material is to small to say anything conclusive.

The average number of ghosts found in the estimated PBG, is also very similar to that of the flat PBG, with an average number of detected ghosts of 0.9. It may have larger fluctuations, especially for strong sources, but further simulations is required to obtain a more quantitative error estimate.

Figure 5.9 shows the average detection level of respectively the sources found in the estimated PBG (fully drawn lines). This plot is very similiar to that for the flat PBG (fig. 5.5), with a linear decrease in the source detection level.

The average detection level of the ghosts in the estimated PBG is also comparable with that of the flat PBG, with an approximately constant ghost detection level a little less than 11.

5.5.1 The smoothed estimated PBG

Similar to the flat PBG, the estimated PBG was smoothed and the results plotted. The results of the smoothing is very similar as when applied to the flat PBG. The average number of identified sources are shown in the left half of figure 5.8 and that of ghosts in the right half.

As with the flat PBG, there are indications that the smoothing may have had a small positive effect on the number of found sources, but the data is not altered significantly.

The number of ghosts, have been very influenced by the smoothing and the average number of ghosts found in a simulation is reduced from an average of 0.9 ghost/simulation to 0.1 ghost/simulation, as for the flat PBG.

The average detection levels, shown in figure 5.9 (found sources) and figure 5.10 (ghosts), shows the same caracteristics as for the flat PBG. There is a tendency for the source detection level to be slightly raised, but this is again not statistically significant. The detection level of the ghosts is almost the same for the smoothed and the un-smoothed estimated PBG, but again there are single peaks in the smoothed image, that are significantly higher.

So far we can conclude that the estimated structured background, does not appear to have a large effect on presence of either the sources or the ghosts. The number of found sources and ghosts is not strongly affected by the shape of the PBG.

We would like to know *how* structured the PBG can be, before it has a major influence on the results. Therefore we attempted to design an extremly structured PBG. This is the subject of the next section.

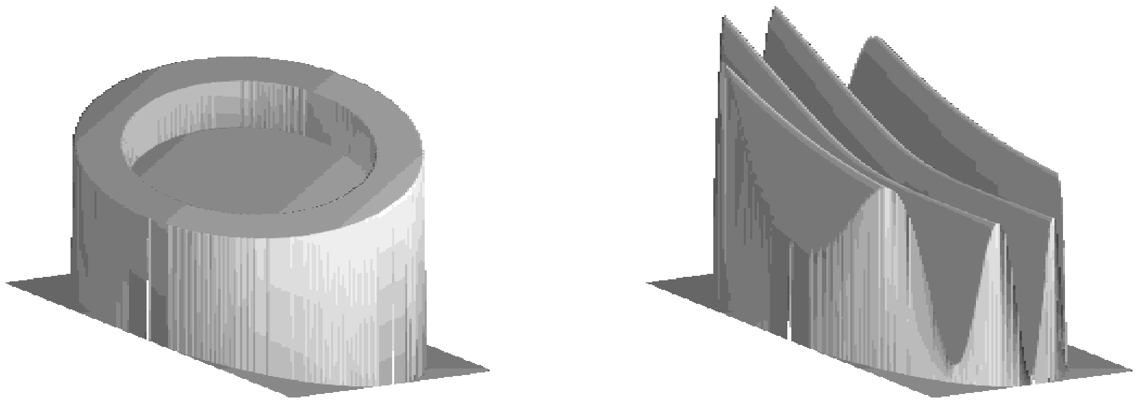

Figure 5.11: *Left:*The distribution probability of the estimated PBG. *Right:* The distribution probability of the extreme PBG.

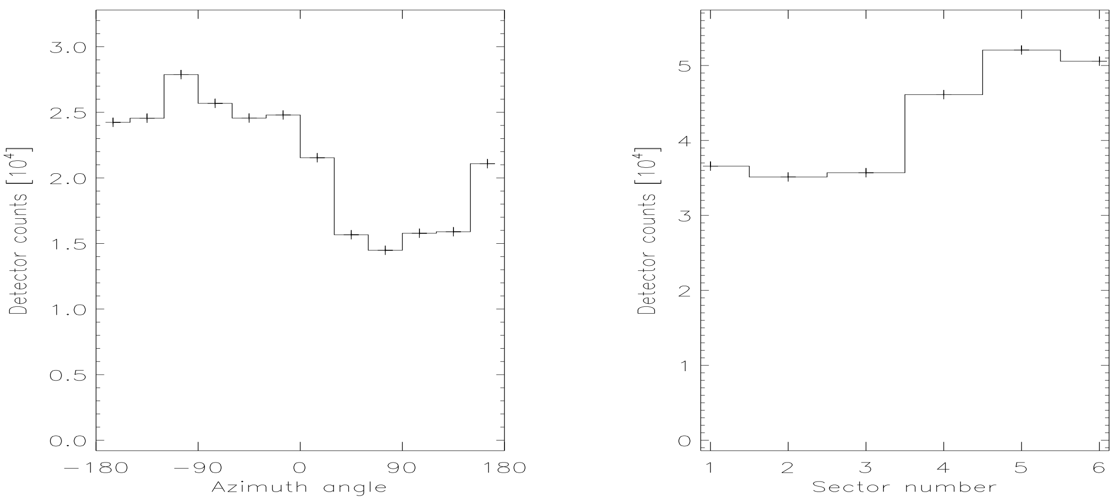

Figure 5.12: The PBG distribution from our extreme model. See e.g. fig. 5.1 right. Errorbars is $\sqrt{(\text{counts})}$. Total nr. of PBG photons is 284579.

5.6 The extreme PBG (JG)

Whether a PBG, which deviates strongly from that by TIMM[2] computed estimate of a PBG distribution, would give rise to radical variations to the previously obtained by the flat PBG and the estimated PBG is investigated.

A sample of various distributions of PBG, with less accordance to the actual or expected nature of CR, were comparised after 25 simulations with four sources of strenght 1.35e-10 erg cm^{-2} s^{-1} for each PBG distribution. The PBG's were chosen to have as large variations over the surface as possibly: saddelforms, spikes, waves etc. - all constructed froma 8 degree polynomium.

In spite of the variete in the PBG's, the results did not differ much. The extreme background distribution, seen as a shade in fig. 5.11, as an excample here did actually yield some of the worst results, as seen from a point of view where many ghost sources is undesireable.

The spectacular of this extreme PBG distribution is the accordance with the estimated PBG (fig. 5.1) in the radial and angular (which if shifted 90^o would be very similar) as seen in fig. 5.12. Interestingly it seems as if this distribution is as good an estimate to the by TIMM computed PBG as the estimated PBG distribution. However there are no physics to support this extreme PBG, as thought Compton scattering[3] in the detector invironment that is as supportive than to the estimated PBG distribution.

By applying the same procedure as for the flat and the estimated PBG, simulations produced the data to create fig. 5.13 and parts of fig. 5.15 and fig. 5.16.

In fig. 5.13 we see a trend with a constant number of sources (allmost 4 pr. simulation i.e. 100% of inserted sources) for source strenghts > 1.3e-10 erg cm^{-2} s^{-1}. And for lower source strenghts the number of sources drops in a smooth curve. In the right side plot the number of ghosts are approximately constant around an average of 1.2 ghosts pr. simulation, which is slightly higher than taht of the flat PBG and the estimated PBG.

[2]See e.g. fig. 5.1 and that discussed in sec. 5.2 [6]

[3]Comptom scattering is usually seen as a ring structure, with very high count level, along the border of the detector. Other X- and γ-ray detectors has experienced such a distribution of the PBG, for example EXITE[1]

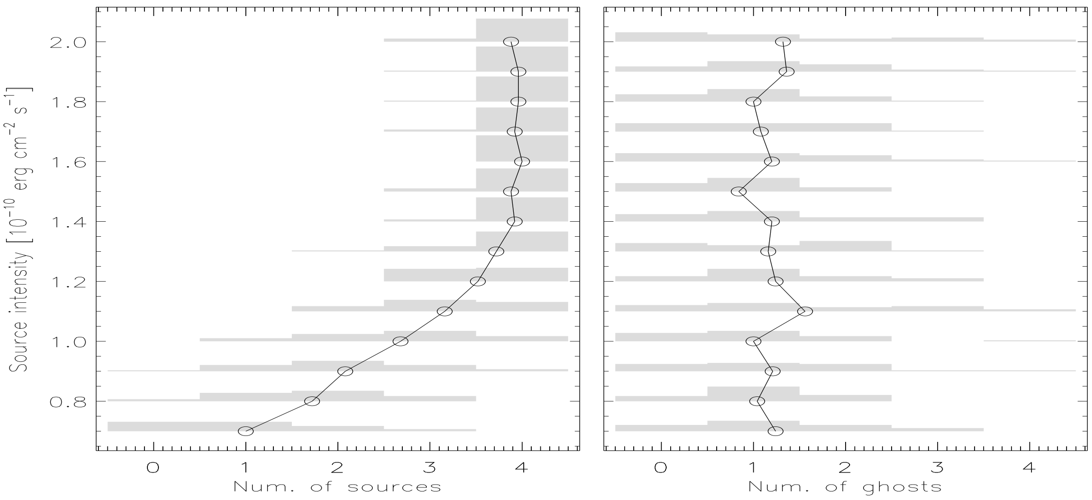

Figure 5.13: Average number of indentified sources (left) and ghosts (right) found in extreme PBG. The histograms behind each point shows the distribution used to calculate each point.

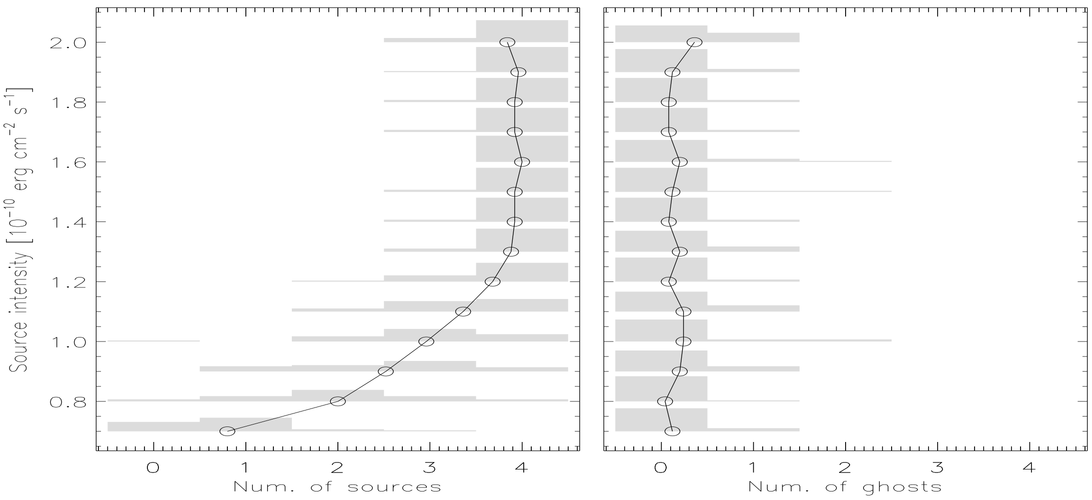

Figure 5.14: Avg. number of sources (left) and ghosts (right) for extreme smoothed PBG.

5.6.1 The smoothed extreme PBG

The extreme PBG was smoothed by the low-pass filter, like the other PBG's.

For the number of sources found (fig. 5.14) after the smoothing there are little or close to no effect, though an improvement in the number of found sources, for source strenghts between 0.8e-10 and 1.3e-10 erg cm^{-2} s^{-1}, is seen. The consequence is a lower cut-off from the constant level (of allmost 4 sources) of sources from source strength 1.4e-10 to 1.3e-10 erg cm^{-2} s^{-1}.

For the number of ghosts (fig. 5.14) there are a significant improvement, by largely reducing all ghosts. The average number of ghosts are 0.2 pr. simulation.

The detection level for the smoothed and the regular cross correlated image for both the sources (fig. 5.15) and the ghosts (fig. 5.16) are plotted. In the plot of detection level for the ghosts the only obvious difference between the smoothed (marked with a dashed line) and the regular (the solid line) are larger fluctuations of detection level for the smoothed ghosts. This may be an effect of the smaller number of found ghosts in the sample after the smoothing. To make good statistics we need a larger amount of data.

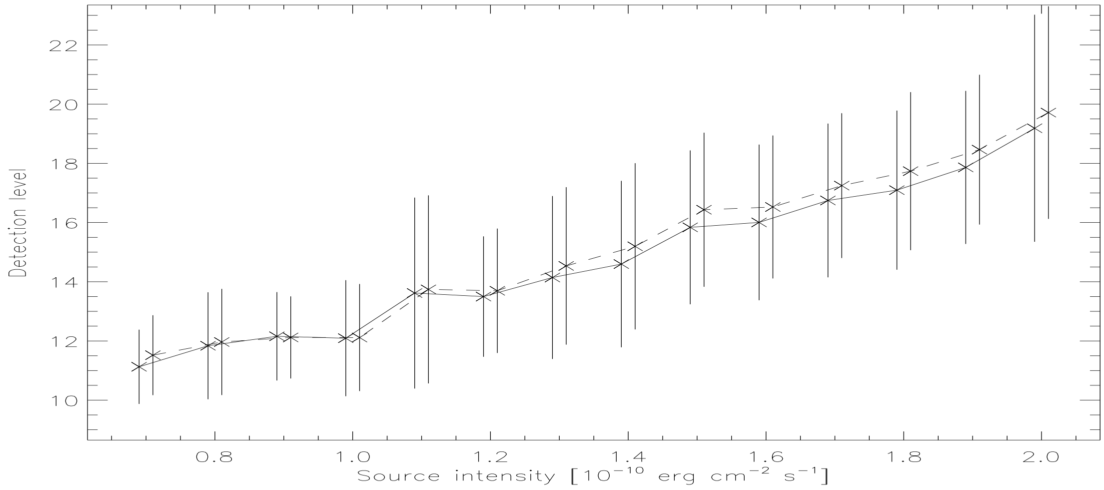

Figure 5.15: Average detection level of indentified soures. The solid line represents the extreme PBG and the dashed line represents the smoothed extreme PBG. Errorbars calculated as RMS.

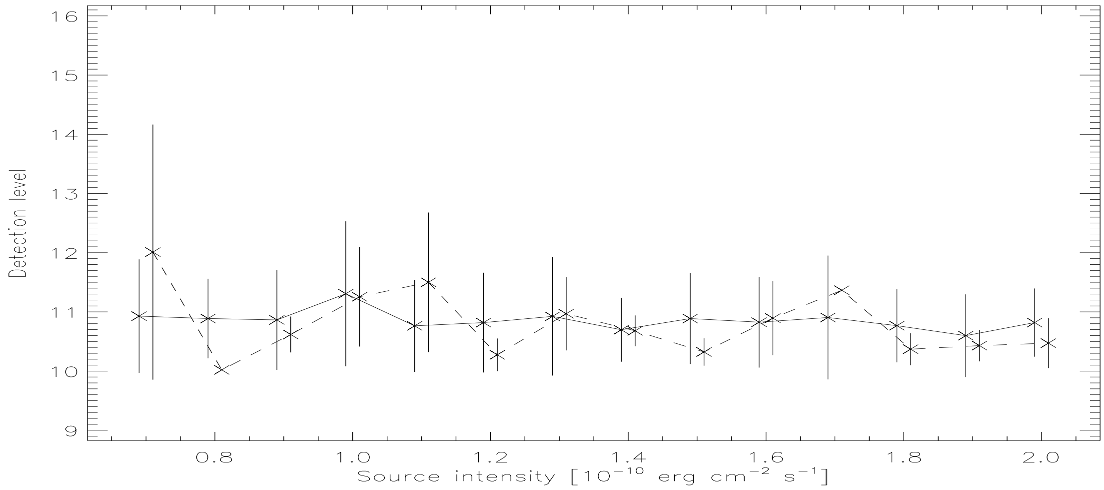

Figure 5.16: Average detection level of ghosts. Solid line represents the extreme PBG and the dashed line represents the smoothed extreme PBG. Errorbars calculated as RMS.

With an average detection level slightly below 11, the ghosts in the extreme background is in accordance with both the flat and the estimated PBG. The trend seen in the smoothed estimated PBG of higher detection level of ghosts for weak sources does, apart from a single ghost, not seem to apply to an arbitrary chosen PBG distribution.

Conserning the sources an effect similar to the one in both the flat and the estimated PBG, with a slightly raised detection level, within the statistics, for source intensities larger than 1.2e-10 erg cm^{-2} s^{-1} in the smoothed image.

The extreme PBG does not seem to give rise to any significant deviations in detection level, than either the flat nor the estimated. And there is a tendency to be an allmost linear dependence between detection level and source intensitiy.

Comparing the results of the extreme PBG with the flat and the estimated PBG, there seems to be only small deviations in the obtained image from the flat PBG and the estimated PBG, and allmost none in the smoothed image.

5.7 Distribution of ghosts (JH + JG)

We have plotted the positions of all input sources, identified sources and ghosts in fig. 5.17.

The identified sources are seen to have a very uniform displacement from the inputted sources, allowing efficient correction for the displacement (see section 2.2.3). However it also shows that it *is* neccesary to correct for this displacement.

The ghosts are plotted using the ghost contribution from *all* of our simulation for *all* PBG's. The ghosts are plotted as dots (expect the dots at distance 125 arcminutes) and shows a surprising distribution. It is evident that the ghosts are distributed in a pattern. Most of the ghosts is close to the edge and furthermore they are primarily positioned in three major spots. This is interesting because it increases the chances to determine which peaks are due to ghosts.

A count of the ghosts shows that $\sim 85\%$ of all ghosts are placed at a distance of more the 288 arcminutes from the center of the image. This is the distance (angle) where the partially illuminated field of view begins, that is, where only part of the detector is illuminated. This region will experience a larger coding noise, so it is not surprising, that more ghosts are found in this area.

The pattern appears to be confining the ghosts to relatively welldefined spots somewhat repeating itself for every 120 degrees. This is almost certainly due to pattern of the mask, that repeats itself for every 120^o. However, the three pattern are not identical and only the major structures can be seen in all three patterns. This is probably due to the complex interaction between the mask and square collimator cells.

This grouping of ghosts can prove to be usefull in rejecting peaks as ghosts. If a peak is found a at position that is known to have a large ghostrate there is high probability that it is a ghost. And because the two masks are orientated differently, many peaks can be rejected, simply by comparing the reconstructed images from the two detectors.

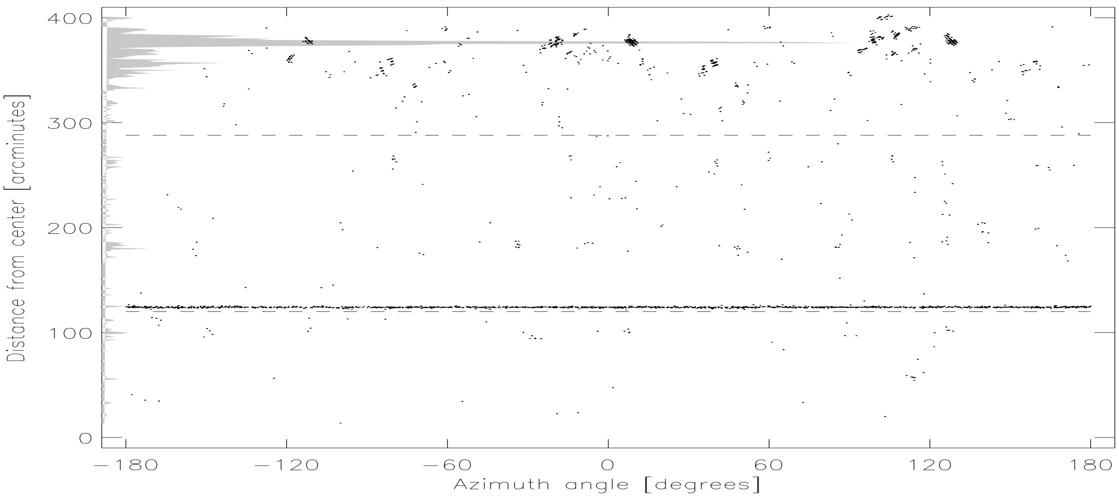

Figure 5.17: Source and ghosts positions as distance and azimuth angle from center of detector. The positions of the input sources are plotted as the dashed line at distance 120 arcminutes. The dots forming a line immediately above represents the positions of the identified sources. All other dots represents the positions of ghosts. The histogram on the distance axis, show the total number of ghosts for a given distance. The dashed line at distance 288 arcminutes, represents where the detector is only partiel illuminated.

Chapter 6

Conclusions (JG + JH)

6.1 The effects of a structured PBG

We have found that a structured PBG has very small effect on the results and generally there is a large degree of correspondense between the flat PBG and the structured PBG's.

The number of found sources are very similar in all three PBG's, especially for strong sources, though there may be small variations for weaker sources. The flat PBG seems to be able to detect more weak sources, but the effect is to small in our results to say anything conclusive and more quantitative investigations is needed to resolve if this is a significant effect.

The number of ghosts is not affected by the estimated PBG. The extreme PBG *does* have a slightly larger ghost count, but the effect is very small and may be statistically insignificant.

The detection levels of sources and ghosts are very similar for all three PBG's and is thus unaffected by a structured PBG.

We therefore conclude that the PBG need to be *very* structured in order to affect the results. We have only been able to see a very small effect when using the most extreme PBG that we could design. Especially does the estimated PBG not have a significant effect.

6.2 The effects of a low-pass filtering (JG + JH)

A low-pass filtering of the shadowgram before reconstruction have proven very significant on the number of ghosts in the reconstructed images. This technique removes approximately 90% of all ghosts but does not affect the number of found sources significally, and if it *does* have an effect on the number of found sources, it is a positive tendency.

There is a tendency for the filtering to raise to detection level of the sources by approximately 0.5. While not significant within the estimated error, this tendency is, however, present for all three PBG's.

The technique seems to introduce a greater variance in the detection level of the ghosts. Especially it introduces some single ghosts with a very high detection level, high enough to be comparable with that of medium strength source. Such single cases with high detection level, is present for all three PBG's. However, these are single cases, hence the statistical material is very small. The mean detection level is, within the errors, very similiar. We have in this project used a detection level threshold of 10, but the average detection level of the ghosts are just below 11. We therefore recommend that this threshold is slightly raised, as most of the ghosts thereby would be rejected. Raising the threshold to 11 would reduce the number of the ghosts we have found by 76% and raising it to 12 would remove 93%. However, raising the detection threshold would also reject some of the weakest true sources.

Because of the dramatic reduction of ghosts, we recommend the use of a filter. The filter that we have applied, has been relatively rough and the results can probably be further improved by better filtering techniques.

6.3 Distribution of ghosts (JG + JH)

The spatial distribution shows significant non-uniformities. The ghosts is grouped along the edge of the reconstructed image in a pattern that is rotated 120^o. A count shows that 85% of all ghosts is found at distances over 288 arcminutes from the center of the image. This increases the chances for rejecting a peak as a ghost significantly. An interesting aspect of the patterne is that one part has much less ghosts then the other two parts. This is probably due to the complex interaction between the coded mask and the collimator. Because the masks are oriented differently, comparing the image from each JEM-X unit combined with a detailed knowledge of the distribution of ghosts may be able to reject a great number of ghosts otherwise accepted as sources. However, further studies are needed to gain knowledge of this relationship.

A great number of simulations with differently oriented masks are required for a more detailed knowledge of this relationship. An examination of the effect that a structured and/or smoothed PBG have on the ghostdistribution could also prove interesting. Analysis of the ghosts in the smoothed background, however, will require a very great number of simulations, since only few ghosts are evident in the reconstructed smoothed images.

A quantitative analysis of the displacement that the souces have would also be desirable. Our results indicates, that a very precise correction can be applied. This is of course desireable in order to obtain more precise skypositions of the sources.

Combining the knowledge of the ghost distribution with smoothing of the background and raising the detection level threshold from 10 to 11, we have estimated that we would be able to reject more than 99% of the found ghosts! This can likely be even further improved by further studies.

6.4 Proposals for further investigation (JG + JH)

For further studies we recomend an investigation of different filtering techniques and the use of other reconstruction methods. In this report we have only applied the cross correlation reconstruction method, but other methods, especially the "Maximum likelihood" method, is promising and may reduce the errors significantly.

Also, we have used input sources, that are placed at a uniform distance from the center. Analyses similar to ours, but with varying number of sources, positions and strengths would be desireable, to determine the relationship between those parameters and the detection of ghosts/sources.

A further study of extremely structured PBG's would also be usefull to determine if it is at all to construct a structured PBG that have a significant effect on the results.

Finally all of the above analyses and proposals would be desireable for energyranges other then 3-20 keV that we have investigated. A structured PBG may have a larger influcence for higher energies, since the DXB is vanishing at high energies, giving the PBG a relative larger influence.

Bibliography

[1] Covault, C.E. *et al*, "Techniques for Removing Non-uniform Background in Coded-Aperture Imaging on the Energetic X-ray Imaging Telescope Experiment", Havard-Smithsonian Center for Astrophysics, April 1991

[2] Goldwurm, Exp. Astron. 6, 9 (1995)

[3] Fenimore, E.E. and Cannon, T.M. "Coded aperture imaging with uniformly redundant arrays", Applied Optics vol. 17, No. 3, February 1978

[4] Fenimore, E.E. and Cannon, T.M. "Uniformly redundant arrays: digital reconstruction methods", Applied Optics vol. 20, No. 10, May 1981

[5] Fenimore, E.E. "Time-resolved and energy-resolved coded aperture images with URA tagging", Applied Optics, Vol. 26, No. 14, July 1987

[6] Feroci, M. *et al*, "The background simulations for the INTEGRAL X-ray monitor JEM-X", Proceedings 3rd INTEGRAL Workshop, Taormina Sept. 1998, in press

[7] Lund, N.,*et al*, "JEM-X: Joint European X-Ray Monitor", Physica Scripta Vol. T77, 39-43, 1998

[8] Malmivaari, K., "Introduction to image reconstruction for coded maks telescopes", 12.11.1997

[9] Rideout, R.M. and Skinner, G.K., "Minimum error image reconstruction for coded mask telescopes", The University of Birmingham, UK, May 1996

[10] Schnopper, H.W. *et al*, "Joint European X-ray Monitor (JEM-X): X-ray monitor for ESA's INTEGRAL mission", SPIE proc. 2806, 1996

[11] Skinner, G.K. and Nottingham, M.R. "Analysis of data from coded-mask telescopes by maximum likelihood", University of Birmingham, UK, March 1993

[12] Westergaard, N.J. (ed.) ,"Background matters for JEM-X", tecnichal document for SDAST internal use, January 27, 1999

[13] Westergaard, N.J. *et al*, "Science with JEM-X", Proceedings INTEGRAL 2nd Workshop, Saint Malo, France, Sept. 1996, ESA SP-382, p605, (1997)

[14] Westergaard, N.J., "Programs and datafiles for JEM-X, Simulation: The JSIM package in F", DSRI 1999

[15] Winkler, C., "INTEGRAL: The International Gamma-Ray Astrophysics Laboratory", INTEGRAL 2nd Workshop, Saint Malo, France, Sept. 1996, ESA SP-382, p573, (1997)

[16] in't Zand, J.,"Coded aperture camera imaging concept", http://lheawww.gsfc.nasa.gov/docs/cai/coded_intr.html, 1992, 1996